Supporting Information

Morphology and Carrier Mobility of high B-content $B_xAl_{1-x}N$ Ternary Alloy from an *Ab Initio* Global search

Zhanbin Qi, Zhiming Shi*, Hang Zang, Xiaobao Ma, Yuxin Yang, Yuping Jia, Ke Jiang, Xiaojuan Sun, and Dabing Li*

Email: shizm@ciomp.ac.cn; lidb@ciomp.ac.cn

1. Benchmark of CALYPSO parameters

1.1 Initial Structures and size of cell

The $B_{0.50}Al_{0.50}N$ system was adapted to test the initial structures and the size of the cell. We set a 30-population size of 50 iterations (30×50=1500) by 20 more iterations than that in our manuscript (30×30=900), and set the sizes of cells of 1(4 atoms), 2(8 atoms), and 4 (16 atoms) formula units, respectively. The results were displayed in Fig S1. The obtained ground structure of $B_{0.50}Al_{0.50}N$ was the same as that in the manuscript. Therefore, the parameters used are reliable enough to the alloy system. On the other hand, we also reviewed the papers using CALYPSO[1-3], the parameters can obtain reliable results.
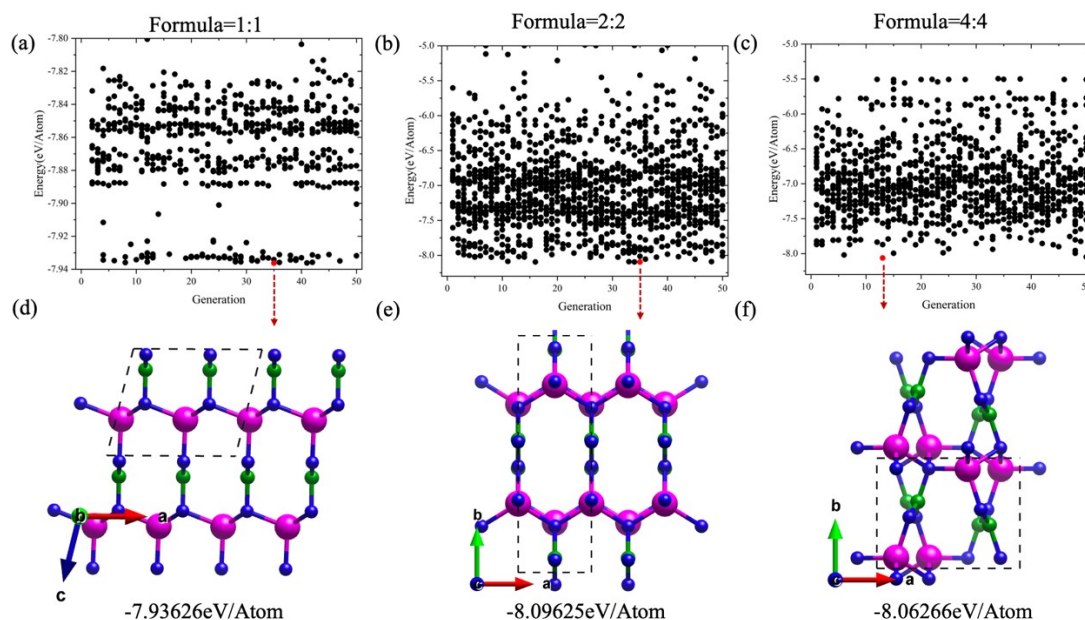
Fig. S1. (a)-(c) Energy evolution of global structure search results versus generations for $B_{0.50}Al_{0.50}N$ with 1500 structures and different size of cell (4, 8, and 16 atoms). (d)-(f) The obtained ground structures for each size of cell.

1.2 Reliability test for the $B_{0.125}Al_{0.875}N$ alloy (low B-content)

The experimental evidence of atomic structures for high B-content alloy is still deficient due to the difficulty of the growth technique. To test the reliability of our calculations, we have searched the ground structures of $B_{0.125}Al_{0.875}N$ alloy (low B-content) and have compared the results with previous experiments. The ground state exhibited a wurtzite structure, meanwhile the zinc-blende structure was also obtained with a quite small energy difference of 4 meV/atom, as shown in Fig S2. Our results agreed with the previous experimental reports.[4,5]
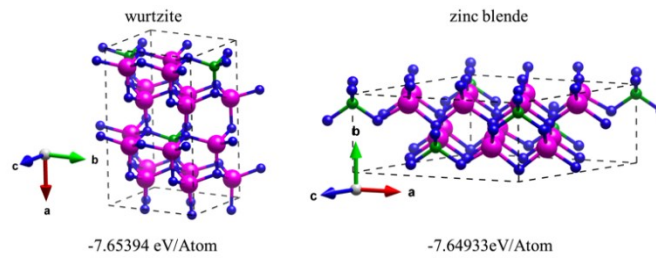
Fig. S2. The ground structures of $B_{0.125}Al_{0.875}N$, the wurtzite (left) and zinc-blende (right). The free energies are marked below.

2. Stability of searched ground structures versus phase separation structures

We adapted a 5nm-wide phase separation $B_xAl_{1-x}N$ structures with different B concentrations as the examples to demonstrate the stability of the searched ground structures. The optimized structures were displayed in Fig S3(a). We find the free energies for these phase separation structures are higher than that for searched ground structures by 16, 90, and 10 meV, respectively. Therefore, the ground structures in this work were more stable than the phase separation structures. Moreover, we have calculated the mixing energy (E_{mixing}) for the $B_xAl_{1-x}N$ system, as shown Fig S3(b). The E_{mixing} for pure III-nitrides were set to zero and connected by the black dashed line (convex hull). We considered the E_{mixing} for the $Al_xGa_{1-x}N$ and $In_xGa_{1-x}N$ systems because these two systems can form stable homogeneous alloys without phase separation in the experiment. We find the E_{mixing} of the $Al_xGa_{1-x}N$ (red circle) and $In_xGa_{1-x}N$ (blue triangle) systems are above the convex hull. For the $B_xAl_{1-x}N$ system (purple ball), we can find similar results to the $Al_xGa_{1-x}N$ and $In_xGa_{1-x}N$ systems. However, the higher E_{mixing} implied the formation of the homogeneous $B_xAl_{1-x}N$ alloys was more difficult than that for the $Al_xGa_{1-x}N$ and $In_xGa_{1-x}N$ systems. The phase separation $B_xAl_{1-x}N$ showed the highest E_{mixing}, indicating the lowest thermodynamic stability than the homogeneous alloys.
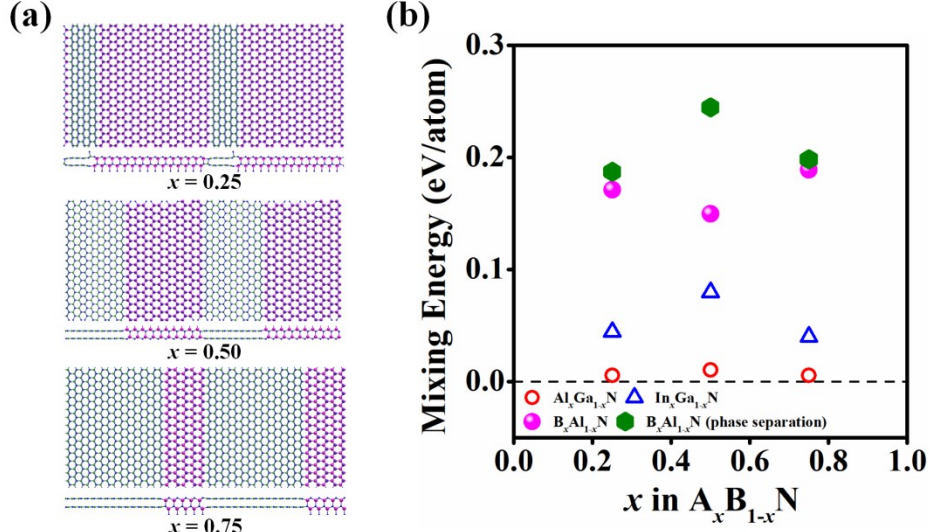
Fig. S3. (a) The optimized phase separation structures for $B_{0.25}Al_{0.75}N$, $B_{0.50}Al_{0.50}N$, and $B_{0.75}Al_{0.25}$ (top to bottom). (b) The mixing energy and convex hull of $Al_xGa_{1-x}N$ (red circle), $In_xGa_{1-x}N$ (blue triangle), $B_xAl_{1-x}N$ (purple ball), and phase separation $B_xAl_{1-x}N$ (green diamond) systems.

3. Linearized Boltzmann Transport Equation

Drift mobility $\mu_{e,\alpha\beta}$ for electron mobility induced by external field E was calculated by the linearized Boltzmann transport equation (BTE) in Eq. (1)

$$\mu_{e,\alpha\beta} = \frac{-1}{n_e\Omega}\Sigma_{n\in CB}\int\frac{dk}{\Omega_{BZ}}v_{nk,\alpha}\partial_{E_\beta}f_{nk},$$
(1)

n_e is electron density, Ω and Ω_{BZ} refer to unit-cell volume and first Brillouin zone. CB refers to conduction bands. $v_{nk,\alpha} = \hbar^{-1}\partial\varepsilon_{nk}/\partial k_\alpha$ and $v_{nk,\alpha}$ refers to group velocity of the band state ε_{nk}, n is band index and k is waver vector. $\partial_{E_\beta}f_{nk}$ is the applied electric field E perturbation item obtained by solving Eq. (2)

$$\partial_{E_\beta}f_{nk} = e\frac{\partial f_{nk}^0}{\partial\varepsilon_{nk}}v_{nk,\beta}\tau_{nk} + \frac{2\pi\tau_{nk}}{\hbar}\Sigma_{mv}\int\frac{dq}{\Omega_{BZ}}|g_{mnv}(k,q)|^2$$
$$\times \left[(n_{qv} + 1 - f_{nk}^0)\delta(\Delta\varepsilon_{k,q}^{nm} + \hbar\omega_{qv})\right.$$
$$\left. + (n_{qv} + f_{nk}^0)\delta(\Delta\varepsilon_{k,q}^{nm} - \hbar\omega_{qv})\right]\partial_{E_\beta}f_{mk+q}.$$
(2)

In equation (2), first term f_{nk}^0 is the equilibrium distribution function and the relaxation time τ_{nk} is shown in Eq. (4). In second term, The matrix elements $g_{mnv}(k,q)$ are shown in Eq. (3) referring to scattering amplitudes between electron initial state *n, k via* phonon with frequency ω_{qv} to final state *m, k+q*. n_{qv} is the Bose-Einstein occupation, f_{nk}^0 is the

equilibrium distribution function and $\Delta\varepsilon_{k,q}^{nm} = \varepsilon_{nk} - \varepsilon_{mk+q}$. For phonon index ω_{qv}, v is branch index, q is crystal momentum.

$$g_{mnv}(k,q) = \left[\frac{\hbar}{2M_\kappa\omega_{qv}}\right]^{1/2}\langle\psi_{mk+q}|\partial_q V|\psi_{nk}\rangle \quad,\qquad(3)$$

M_κ is the atom mass and $\partial_q V$ derives from self-consistent potential associated with wave vector q phonon. ψ_{nk} refers to electronic wave function with band index *n and* wave vector *k*.

$$
\begin{aligned}
\frac{1}{\tau_{nk}} \quad = \quad & \frac{2\pi}{\hbar}\Sigma_{mv\sigma}\int\frac{dq}{\Omega_{BZ}}|g_{mnv}(k,q)|^2 \\
& \times\Big[\left(n_{qv} + 1 - f_{mk+q}^0\right)\delta\left(\Delta\varepsilon_{k,q}^{nm} - \hbar\omega_{qv}\right) \\
& + \left(n_{qv} + f_{mk+q}^0\right)\delta\left(\Delta\varepsilon_{k,q}^{nm} + \hbar\omega_{qv}\right)\Big] \quad,
\end{aligned}
\qquad(4)
$$

After calculating matrix elements $g_{mnv}(k,q)$ in Eq. (3), EPW computes Eq. (4) then solve Eq. (2) and use results in Eq (1). Iterated by generations, electron and hole mobility can be calculated the through BTE method; Omitting second term of Eq. (2), self-energy relaxation time approximation (SETRTA) is deduced, and a no iteration-demand mobility is given in Eq. (5). All the details in drift mobility theory can be found in Review paper from Samuel Poncé et al.[6]

$$\mu_{e,\alpha\beta}^{SERTA} = \frac{e}{n_e\Omega}\Sigma_{n\in CB}\int\frac{dk}{\Omega_{BZ}}\frac{\partial f_{nk}^0}{\partial\varepsilon_{nk}}v_{nk,\alpha}v_{nk,\beta}\tau_{nk} \quad.\qquad(5)$$

4. Electron and Phonon parameter of w-AlN, h-BN and $B_xAl_{1-x}N$
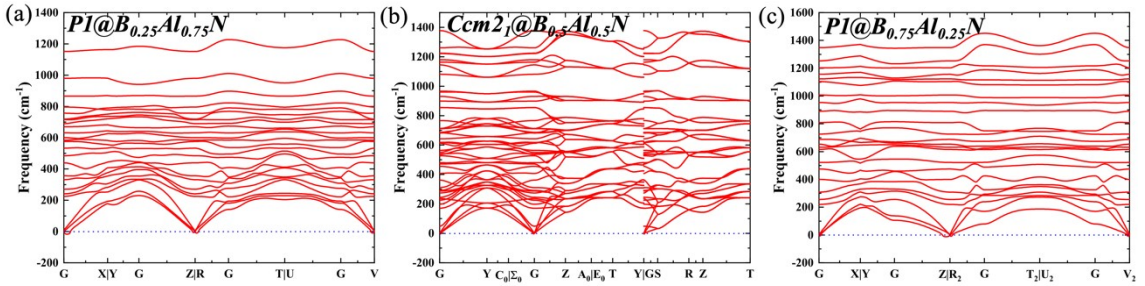
Fig. S4. Phonon spectrum of (a) P1@ $B_{0.25}Al_{0.75}N$, (b)Ccm2$_1$@ $B_{0.5}Al_{0.5}N$, and (c)P1@ $B_{0.75}Al_{0.25}N$.
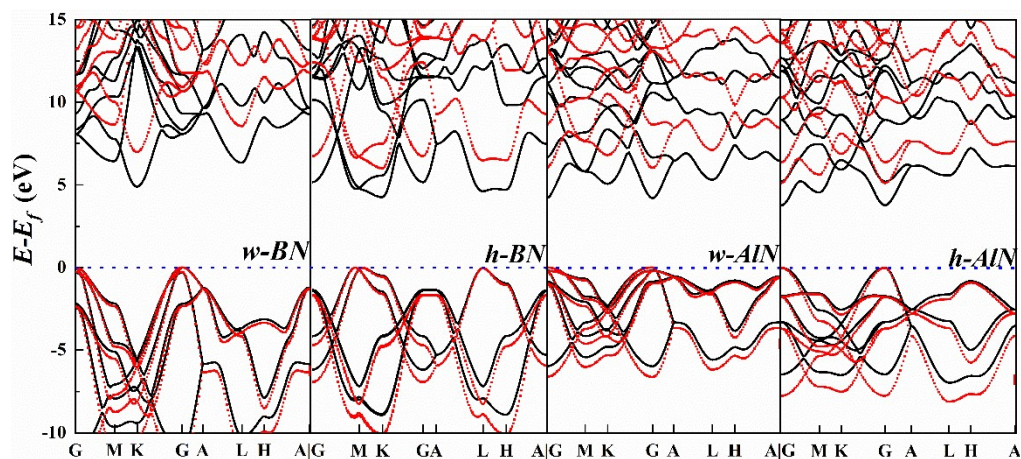
Fig. S5. Band Structures of wurtzite and hexagonal structures w-BN, h-BN, w-AlN, h-AlN obtained at PBE (black solid lines) and HSE06 (red dashed lines) levels.
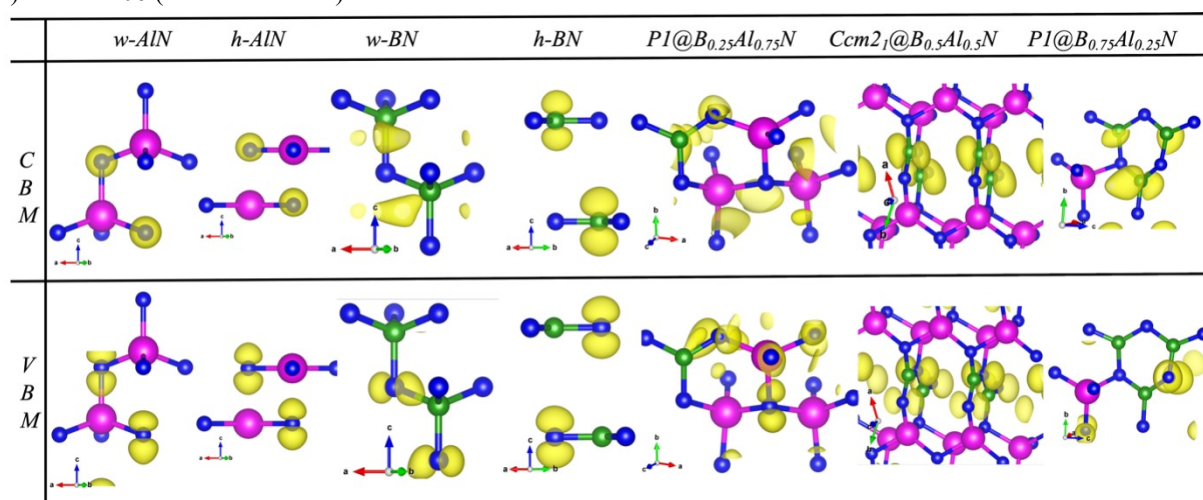
Fig. S6. Spatial distributions of the squared wave function for CBM and VBM in wurtzite BN and hexagonal AlN structures. Besides, wave functions for $B_xAl_{1-x}N$ alloy searched results are also shown. The purple, green, and blue spheres represent the Al, B, and N atoms.

Searched Structure	Space Group	Lattice Parameter (Å, °)	Atoms	x	y	z
$B_{0.25}Al_{0.75}N$	P1	a=3.118(88.54°)	Al1	0.39094	0.71842	0.73570
		b=4.787(87.50°)	Al2	0.90327	0.73142	0.21995
		c=5.212(87.29°)	Al3	0.38578	0.22938	0.39401
			B1	0.00049	0.25269	0.92483
			N1	0.89884	0.56631	0.89642
			N2	0.26531	0.10521	0.73369
			N3	0.40125	0.62287	0.39195
			N4	0.90841	0.12700	0.19392
$B_{0.5}Al_{0.5}N$	$Ccm2_1$	a=3.205 (90°)	Al1	0.00000	0.21076	0.87756
		b=10.351(87.50°)	Al2	0.50000	0.28924	0.37756
		c=4.670 (87.29°)	Al3	0.50000	0.71076	0.87756
			Al4	0.00000	0.78924	0.37756
			B1	0.50000	0.44104	0.85932
			B2	0.50000	0.55896	0.35932
			B3	0.00000	0.94104	0.85932
			B4	0.00000	0.05896	0.35932
			N1	0.50000	0.30406	0.97488
			N2	0.00000	0.19594	0.47488
			N3	0.50000	0.44939	0.54857
			N4	0.50000	0.55061	0.04857
			N5	0.00000	0.80406	0.97488
			N6	0.50000	0.69594	0.47488
			N7	0.00000	0.94939	0.54857
			N8	0.00000	0.05061	0.04857
$B_{0.75}Al_{0.25}N$	P1	a=3.238 (89.94°)	Al1	0.15161	0.51277	0.12728
		b=4.504 (76.55°)	B1	0.43728	0.97325	0.31984
		c=5.150 (80.44°)	B2	0.35855	0.97627	0.81777
			B3	0.43033	0.47794	0.57091
			N1	0.33204	0.10685	0.08431
			N2	0.55455	0.63339	0.31440
			N3	0.41265	0.15069	0.56815
			N4	0.30550	0.66655	0.80307

Table.S1. Atom Positions and Lattice parameters of searched structures $B_{0.25}Al_{0.75}N$, $B_{0.5}Al_{0.5}N$ and $B_{0.75}Al_{0.25}N$.

	w-AlN	w-AlN ref[7-9]	h-AlN	h-AlN ref[10,11]	$B_{0.25}Al_{0.75}N$	$B_{0.5}Al_{0.5}N$	$B_{0.75}Al_{0.25}N$	w-BN	w-BN ref[9]	h-BN*	h-BN ref[9]*
a(Å)	3.11	3.11	3.30	3.30	3.12	3.21	3.24	2.55	2.54	2.51	2.49
b(Å)					4.79	10.35	4.50				
c(Å)	4.99	4.98	4.16	4.16	5.21	4.67	5.15	4.21	4.20	6.71	6.66
Bandgap	Dir	Dir	Dir	Dir	Indir	Indir	Indir	Indir	Indir	Indir	Indir
PBE (eV)	4.19		3.78		3.81	1.99	2.68	4.89		4.26	
HSE (eV)	6.02		5.12		5.48	3.52	4.31	6.98		6.01	
Bravais-Type	Hexagonal				Triclinic	Orthorhombic	Triclinic	Hexagonal		Hexagonal	
$me^{\perp}$ **unit(m_o)**	0.34	0.31/0.35/0.30	0.31	0.36	1.90(ZU)/0.51(ZT)	0.82(SY)/0.73(SG)	0.92(U_2Z)/0.52(U_2R_2)	0.511	0.35	0.257	0.26
$me^{\parallel}$	0.33	0.32/0.32	0.33		17.53(ZG)	0.42 (SR)	6.23(U_2X)	0.31	0.24	2.95	2.21
$m_{hh}^{\perp}$	16.39	11.11/11.14	0.93	0.92	3.96(XG)	0.77(GS_0)/25.37(GY)	1.67(ZU_2)/1.37(ZT_2)	1.34	1.02	0.69	0.50
$m_{hh}^{\parallel}$	3.58	2.94/3.53	0.28		0.92(XU)	0.65(GZ)	2.15(ZG)	1.28	1.08	1.59	1.33
$m_{lh}^{\perp}$	0.30	0.26/0.33									
$m_{lh}^{\parallel}$	3.57	2.94/3.53									
$m_{sh}^{\perp}$	4.66	3.57/4.05									
$m_{sh}^{\parallel}$	0.25	0.25/0.26									

Table.S2. Electron and hole effective masses for w-AlN, h-AlN, w-BN, hBN and selected BAlN structures $m^{\parallel}$ and $m^{\perp}$ referring to effective mass along high symmetry path along kz and kx directions and me, m_{hh}, m_{lh} and m_{sh} refer to electron, heavy hole band, light hole band and split hole band for each row. * $m_{hh}^{\perp}$ and $m_{hh}^{\parallel}$ of h-BN refer to M to Gamma and M to L in first brillouin zone.

5. Phonon structure of NEB final four coordinated structures and their imaginary phonon mode at gamma
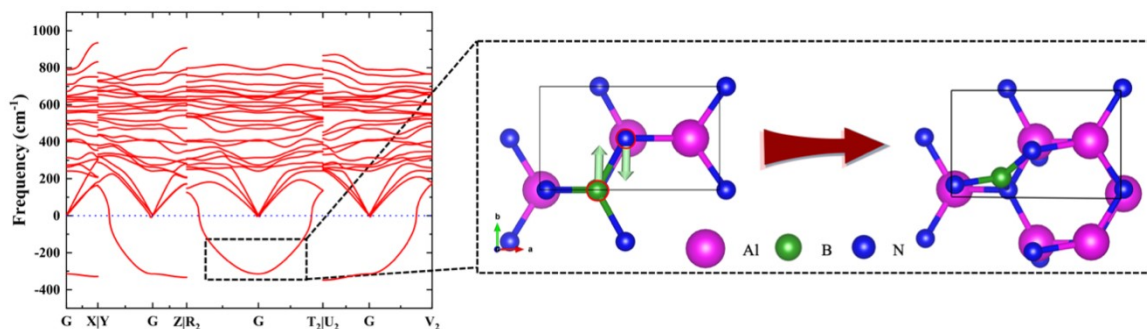
Fig. S7. Calculated phonon spectrum for $B_{0.25}Al_{0.75}N$, the vibration mode for the imaginary frequency is highlighted by dashed box. The purple, green, and blue spheres represent the Al, B, and N atoms.

Here we selected final state of four coordinated B structures and calculated their phonon spectra. The phonon vibrational modes at Gamma showed largest imaginary frequency and we visualized relative atom vibration. For P1@ $B_{0.25}Al_{0.75}N$, imaginary vibration at gamma was related with relative movement of B atom and N shown in top view. The relative movement of B and N atom along b direction broke four coordinated structure of B atom and formed 3 coordinated one.

6. Quantum Espresso relaxation results and EPW mobility details
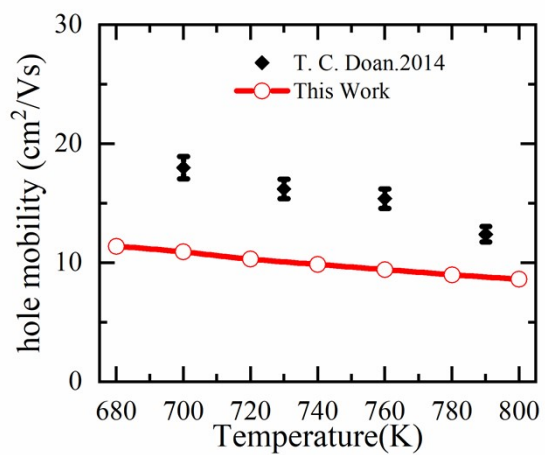
Fig. S8. Mobility of h-BN calculated from 680K to 800K (red line), and experiment results are shown in error bar (black bar). We calculated hole mobility from 680K to 800K in reasonable range of values compared with Ref mobility[12] for hole mobility in intrinsic h-BN.
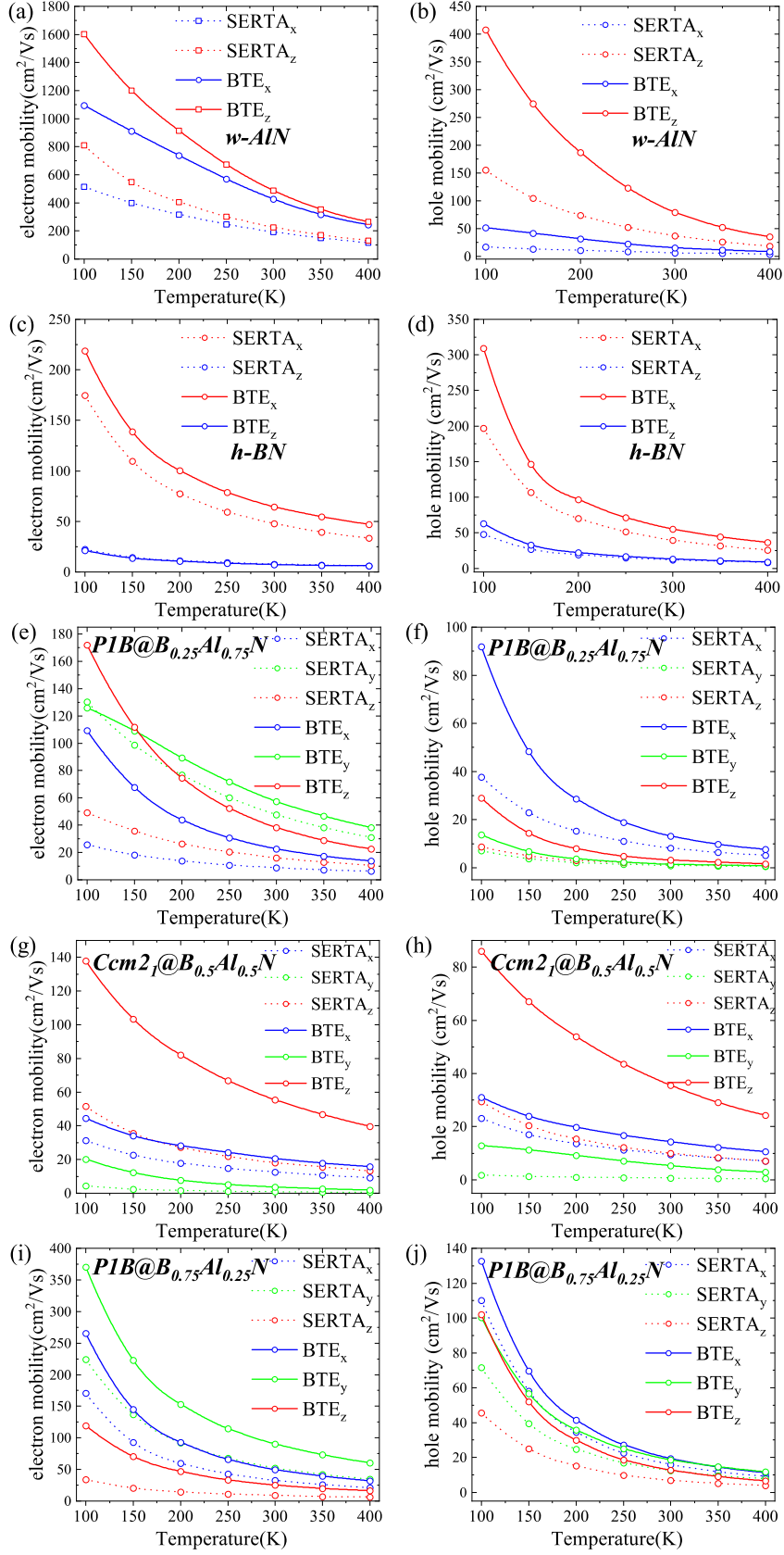
Fig. S9. Electron and hole intrinsic drift mobilities in three directions of (a)(b) w-AlN, (c)(d) hBN, (e)(f) P1@B$_{0.25}$Al$_{0.75}$N, (g)(h) Ccm2$_1$@B$_{0.5}$Al$_{0.5}$N, (i)(j) P1@B$_{0.75}$Al$_{0.25}$N and versus temperature from 100K to 400K.

Mobility of w-AlN showed anisotropy in x z directions and isotropy in x y directions and we just showed mobility in x and z directions in Fig. S9(a)(b). The same was true in Fig. S9(c)(d) for h-BN. For the rest B contents-$B_{0.25}Al_{0.75}N$, $B_{0.5}Al_{0.5}N$ and $B_{0.75}Al_{0.25}N$, due to strong anisotropy in three directions, SERTA and BTE mobilities in all directions were shown.

For w-AlN BTE(SERTA) electron mobility in z-axis direction was 1.47(1.58) times of x-axis direction at 100K ,1.14(1.18) at 300K and 1.09(1.13) at 400K. For hole, BTE(SERTA) mobility in z-axis direction was 7.95(9.24) times of x-axis direction at 100K, 5.15(5.92) at 300K and 4.32(4.87) at 400K.

For h-BN BTE(SERTA), due to interlayer van der Waals force, carriers transport along z-axis was difficult compared with x, y in-layer directions, which was shown in Fig. S9(c)(d). Electron mobility in x-axis was 10.37 (7.84) times of z-axis direction at 100K, 8.73 (6.11) at 300K and 8.13 (5.59) at 400K.For hole, BTE(SERTA) mobility in x-axis direction was 4.91(4.09) times of z-axis direction at 100K and 4.19(3.34) at 300K and 4.04(3.12) at 400K. Different from w-AlN, it was found intrinsic hole mobility was about 1.5(1.2) times of electron mobility at 100K. Electron and hole mobilities were comparable when temperature was above 200K.

For P1@$B_{0.25}Al_{0.75}N$, electron mobility dominantly contributed from z and y direction. For hole mobility, most mobility contribution in x direction was 9.24(8.99) times of y direction and 4.16(5.60) times of z direction at 300K.

Anisotropy in carrier mobility of Ccm2$_1$@$B_{0.5}Al_{0.5}N$-ten-membered ring was defined to be strongest in three selected structure shown in Fig. S9(g)(h). For Ccm2$_1$@ $B_{0.5}Al_{0.5}N$ dominant contribution part was in z direction. And x direction contributed secondly which was 1/2.69(1.46) of z direction in BTE(SERTA) for electron and 1/2.49(1.05) for hole at 300K.The least contribution came from y direction which was 1/16.15(24.87) of z direction for election and 1/6.77(15.88) for hole at 300K.

For P1@$B_{0.75}Al_{0.25}N$, Here we also found mobility showed similar anisotropy as h-BN. Mobility in z-direction contributed the least part compared with in-plane contributions. Three directions contributed equally to total mobility. Y direction contributed mostly for electron and x direction for hole. BTE(SERTA) electron mobility results of Y direction were 1.82(1.63) times of x direction contribution and 3.58(6.19) times of z direction at 300K.For hole, x direction was 1.03(1.28) of y direction contribution and 1.53(2.32) of z direction at 300K.It was found mobility in z-direction was least contribution part compared with the other directions.

	VASP			QE		
	a	b	c	a	b	c
AlN	3.114(90)	3.114(90)	4.992(120)	3.108(90)	3.108(90)	4.983(120)
P1@B$_{0.25}$Al$_{0.75}$N	3.118(88.54)	4.787(87.50)	5.212(87.29)	3.093 (88.60)	4.743(87.60)	5.169 (87.45)
Ccm2$_1$@B$_{0.5}$Al$_{0.5}$N	3.205(90)	10.351(90)	4.670(90)	3.177 (90)	10.253 (90)	4.627 (90)
P1@B0$_{.75}$Al$_{0.25}$N	3.238(89.94)	4.504(76.55)	5.150(80.44)	3.190 (89.90)	4.457 (76.78)	5.098(80.52)
hBN	2.509(90)	2.509 (90)	6.710(120)	2.482(90)	2.482(90)	6.413(120)

Table.S3. Lattice parameters a, b, c(Å) and three angles (α°, β°, γ°) results relaxed from VASP and QE.

	Ecut (Ry)	Coarse k	q	wannier interpolation	WF	Spread (Å^2)	k-grid	q-grid	Mobility@300K(cm^2/(V*S))
wAlN-e	80	6^3	6^3	90^3	16	1.938	129780	729000	445.36
wAlN-h	-	-	-	60^3	-	-	39720	216000	36.67
P1@B$_{0.25}$Al0$_{.75}$N -e	80	8*5*5	8*5*5	48*30*30	28	2.226	86400	43200	39.37
P1@B$_{0.25}$Al0$_{.75}$N -h	-	-	-	-	-	-	-	-	5.92
Ccm2$_1$@B$_{0.5}$Al$_{0.5}$N-e	80	8^3	4^3	48^3	28	2.461	57696	110592	26.48
Ccm2$_1$@B$_{0.5}$Al$_{0.5}$N-h	-	-	-	-	-	-	-	-	18.31
P1@B0$_{.75}$Al$_{0.25}$N -e	50	8*5*5	8*5*5	56*35*35	28	2.429	137200	68600	54.97
P1@B0$_{.75}$Al$_{0.25}$N -h	-	-	-	48*30*30	-	-	86400	43200	16.78
hBN-e	80	8*8*6	8*8*6	60^3	16	1.996	20522	216000	45.44
hBN-h	-	-	-	60^3	-	-	-	-	41.29

Table.S4. Planewaves kinetic energy cutoff, coarse Brillouin grid for scf and phonon calculations, dense grid described by wannier interpolation parameter, wannier function numbers and wannier spread per function, total size of k/q mesh for interpolation and averaged BTE mobility on three directions @300K.

REFERENCES

[1] Yu Wang, Feng Li, Yafei Li, and Zhongfang Chen,   Nature communications **7** (1), 1 (2016).

[2] Miao Zhang, Hanyu Liu, Quan Li, Bo Gao, Yanchao Wang, Hongdong Li, Changfeng Chen, and Yanming Ma,   Phys. Rev. Lett. **114** (1), 015502 (2015).

[3] Xin Zhong, Hui Wang, Jurong Zhang, Hanyu Liu, Shoutao Zhang, Hai-Feng Song, Guochun Yang, Lijun Zhang, and Yanming Ma,   Phys. Rev. Lett. **116** (5), 057002 (2016).

[4] X. Li, S. Wang, H.x. Liu, Fernando A. Ponce, T. Detchprohm, and R.D. Dupuis,   Phys. Status Solidi B **254** (8), 1600699 (2017).

[5] X. Li, S. Sundaram, Y. El Gmili, T. Moudakir, F. Genty, S. Bouchoule, G. Patriarche, R. D. Dupuis, P. L. Voss, J. P. Salvestrini, and A. Ougazzaden,   Phys. Status Solidi A **212** (4), 745 (2015).

[6] S. Ponce, W. Li, S. Reichardt, and F. Giustino,   Rep. Prog. Phys. **83** (3), 036501 (2020).

[7] A. Punya and W.R. Lambrecht,   Phys. Rev. B **85** (19), 195147 (2012).

[8] K. Kim, W. R. L. Lambrecht, B. Segall, and M. vanSchilfgaarde,   Phys. Rev. B **56** (12), 7363 (1997).

[9] Y. N. Xu and W. Y. Ching,   Phys. Rev. B: Solid State **44** (15), 7787 (1991).

[10] Y. Cai, Y. Liu, Y. Xie, Y. Zou, C. Gao, Y. Zhao, S. Liu, H. X. Xu, J. Shi, S. S. Guo, and C. L. Sun,   APL Mater. **8** (2), 021107 (2020).

[11] C. E. Dreyer, A. Janotti, and C. G. Van de Walle,   Appl. Phys. Lett. **102** (14), 142105 (2013).

[12] T. C. Doan, J. Li, J. Y. Lin, and H. X. Jiang,   AIP Adv. **4** (10), 107126 (2014).